



# Characterization of ion track-etched conical nanopores in thermal and PECVD SiO<sub>2</sub> using small angle X-ray scattering

Shankar Dutt<sup>\*1</sup>, Rudradeep Chakraborty<sup>1</sup>, Christian Notthoff<sup>1</sup>, Pablo Mota-Santiago<sup>2</sup>, Christina Trautmann<sup>3,4</sup> and Patrick Kluth<sup>1</sup>

## Full Research Paper

Open Access

Address:

<sup>1</sup>Department of Materials Physics, Research School of Physics, The Australian National University, Canberra ACT 2601, Australia,  
<sup>2</sup>ANSTO-Australian Synchrotron, Clayton VIC 3168, Australia, <sup>3</sup>GSI Helmholtzzentrum für Schwerionenforschung, Planckstr. 1, 64291 Darmstadt, Germany and <sup>4</sup>Technische Universität Darmstadt, 64289 Darmstadt, Germany

Email:

Shankar Dutt\* - shankar.dutt@anu.edu.au

\* Corresponding author

Keywords:

etched ion tracks; SiO<sub>2</sub>; small angle X-ray scattering (SAXS); swift heavy ion irradiation; track-etched nanopores

*Beilstein J. Nanotechnol.* **2025**, *16*, 899–909.

<https://doi.org/10.3762/bjnano.16.68>

Received: 19 February 2025

Accepted: 22 May 2025

Published: 12 June 2025

This article is part of the thematic issue "Energetic ions and photons for engineering nanomaterials".

Guest Editor: V. R. Soma



© 2025 Dutt et al.; licensee Beilstein-Institut.

License and terms: see end of document.

## Abstract

Conical nanopores in amorphous SiO<sub>2</sub> thin films fabricated using the ion track etching technique show promising potential for filtration, sensing, and nanofluidic applications. The characterization of the pore morphology and size distribution, along with its dependence on the material properties and fabrication parameters, is crucial to designing nanopore systems for specific applications. Here, we present a comprehensive study of track-etched nanopores in thermal and plasma-enhanced chemical vapor-deposited (PECVD) SiO<sub>2</sub> using synchrotron-based small-angle X-ray scattering (SAXS). The nanopores were fabricated by irradiating the samples with 89 MeV, 185 MeV, and 1.6 GeV Au ions, followed by hydrofluoric acid etching. We present a new approach for analyzing the complex highly anisotropic two-dimensional SAXS patterns of the pores by reducing the analysis to two orthogonal one-dimensional slices of the data. The simultaneous fit of the data enables an accurate determination of the pore geometry and size distribution. The analysis reveals substantial differences between the nanopores in thermal and PECVD SiO<sub>2</sub>. The track-to-bulk etching rate ratio is significantly different for the two materials, producing nanopores with cone angles that differ by almost a factor of two. Furthermore, thermal SiO<sub>2</sub> exhibits an exceptionally narrow size distribution of only 2–4%, while PECVD SiO<sub>2</sub> shows a higher variation ranging from 8% to 18%. The impact of different ion energies on the size of the nanopores was also investigated for pores in PECVD SiO<sub>2</sub> and shows only negligible influence. These findings provide crucial insights for the controlled fabrication of conical nanopores in different materials, which is essential for optimizing membrane performance in applications that require precise pore geometry.

## Introduction

Solid-state nanopores have attracted significant attention in the past decade because of their broad applicability in a variety of areas including biosensing, micro/ultrafiltration, desalination, ion and molecular separation, dialysis, battery technologies, blue energy generation, and nanofluidics [1-33]. Conical nanopores are of particular interest because of the asymmetric ion transport resulting from their unique geometry [30,34-38].

Conical nanopores can be reproducibly fabricated at scale using the track-etch technology in a number of different materials [29,39]. This method involves irradiating the material with swift heavy ions to create long and narrow damaged regions along the paths of the ions known as “ion tracks”. These ion tracks are more susceptible to chemical etching compared to the undamaged material, which can be exploited for the fabrication of nanopores with narrow size distribution [13,29,40]. The geometry of the resulting nanopores is determined by several factors, including the substrate material, the type and concentration of the etchant, the density of the material, and the type and energy of the ions used [13,29,40].

Track-etch technology has been used for the commercial fabrication of cylindrical nanopores in polymers for filtration applications [41-46]. Only recently we have adapted this technology to generate conical nanopores in silicon dioxide [29,30,40]. Amorphous silicon dioxide ( $\text{SiO}_2$ ) has excellent chemical stability, well-understood surface chemistry, and compatibility with semiconductor processing, opening up new applications for track-etched nanopores in this material [30].

In this study, we report the characterization of track-etched nanopores in two types of silicon dioxide, namely, one produced by wet thermal oxidation of Si (thermal  $\text{SiO}_2$ ) and another deposited by plasma-enhanced chemical vapor deposition (PECVD). Thermally grown  $\text{SiO}_2$  is of high quality and stoichiometric, however, requires high temperatures for growth, and can only be grown on a Si substrate. PECVD, in contrast, allows for the deposition at much lower temperatures on many different substrates with control over the film properties, such as stoichiometry, density, refractive index, and residual stress. As these fabrication methods involve fundamentally different growth mechanisms, the resulting layers have different properties [47,48] and it can be expected that the track-etched nanopores also show different characteristics, including the track etching process itself. Understanding how the different fabrication methods influence the characteristics of ion track-etched nanopores is crucial to optimize their fabrication for specific applications. Here we focus on characterizing size, geometry, and size distribution of track-etched nanopores in thermal and PECVD  $\text{SiO}_2$  as these parameters are critical for mem-

brane performance in specific applications, including selectivity, throughput, and molecular capture.

Small-angle X-ray scattering (SAXS) has proven to be an invaluable tool for characterizing nanopore membranes, offering nondestructive analytical capabilities that yield statistical information of more than  $10^6$  pores [6,13,29,40]. With a beam size at the Australian Synchrotron of  $250 \text{ }\mu\text{m} \times 23 \text{ }\mu\text{m}$ , we measure  $\approx 5.8 \times 10^5$  and  $\approx 2.9 \times 10^6$  nanopores for samples irradiated with fluences of  $1 \times 10^8$  and  $5 \times 10^8 \text{ ions/cm}^2$ , respectively. Our previous work demonstrated the effectiveness of SAXS for studying conical nanopores in  $\text{SiO}_2$ , providing unprecedented precision in determining the pore morphologies [29,40]. The method involved fitting two-dimensional (2D) scattering patterns to a conical pore model utilizing a series of images with different tilts of the sample with respect to the incident X-ray beam, corresponding to the alignment of the parallel pores with the beam. Although highly accurate, this approach has two limitations, that is, the computational resources required for numerical calculation of intensity values for each pixel in the 2D fit and the challenge of incorporating size distribution analysis due to the computational complexity of applying distribution functions in a 2D fitting scenario. To address these limitations, we have developed a new approach that maintains the high precision of SAXS analysis while significantly reducing computational requirements and enabling the investigation of size distributions. This method involves analyzing and fitting one-dimensional (1D) sections of the SAXS patterns employing different form factors rather than performing 2D image fitting.

We implemented our new fitting method to investigate conical nanopores in the two different  $\text{SiO}_2$  membrane materials. For nanopores in thermal  $\text{SiO}_2$  we confirm that these results are consistent with our previous studies that employ 2D fitting and quantify the size distribution. Track-etched nanopores in PECVD- $\text{SiO}_2$  have not been studied before and revealed striking differences in the geometrical parameters due to a different track-to-bulk etching rate ratio and a wider size distribution.

## Results and Discussions

Figure 1 shows plan-view scanning electron microscopy (SEM) images of nanopores fabricated in thermal (Figure 1a) and PECVD (Figure 1b)  $\text{SiO}_2$  by etching ion tracks produced with 1.6 GeV Au ion irradiation (see Experimental and Theory section for details). Although both materials reveal conical nanopores, thermal  $\text{SiO}_2$  exhibits more uniformly sized nanopores, while PECVD  $\text{SiO}_2$  displays higher dispersity in pore dimensions (excluding overlapping pores). As an example,

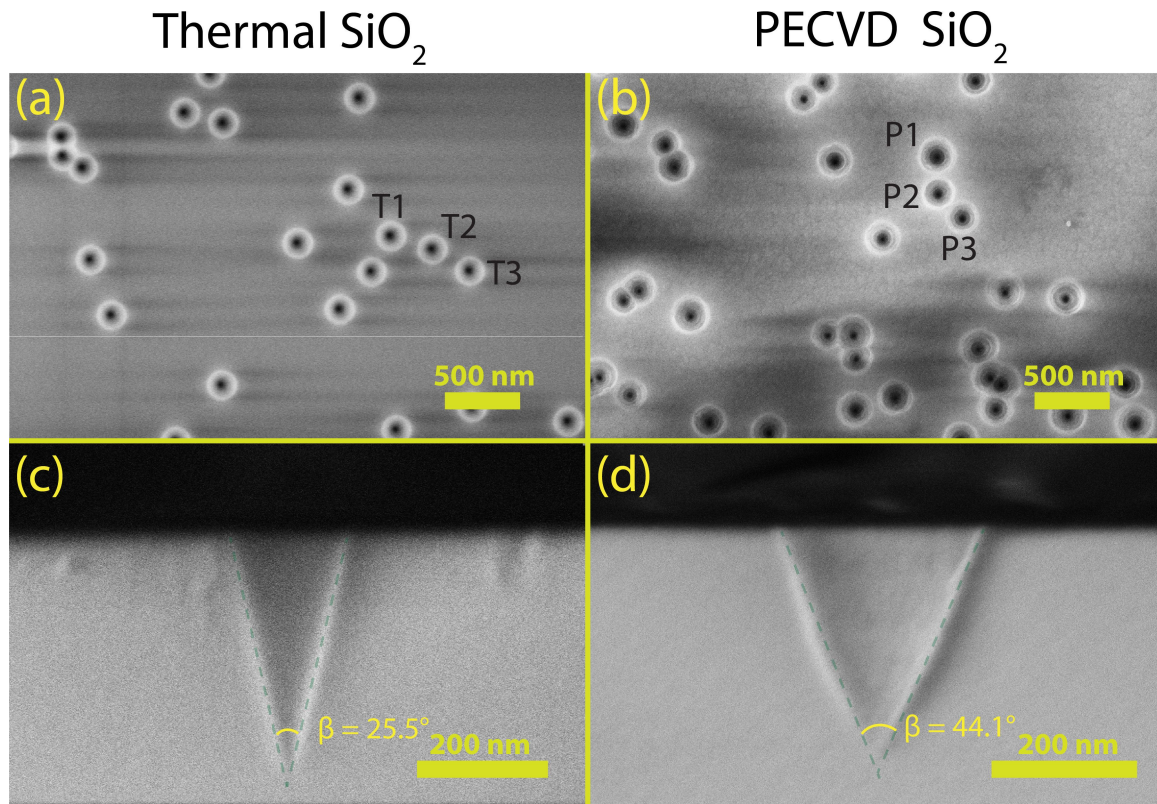


**Figure 1:** Plan-view (a, b) and cross-sectional (c, d) scanning electron microscopy images of nanopores in thermal (a, c) and PECVD (b, d)  $\text{SiO}_2$ . The thermal and PECVD  $\text{SiO}_2$  thin films were irradiated with 1.6 GeV Au ions and subsequently etched in 3% HF for 8.5 min and 6 min respectively. The irradiation fluence was  $5 \times 10^8 \text{ ions/cm}^2$ . The fluence was verified by counting nanopores in multiple SEM images, closely matching the expected values. The top-view images (a, b) highlight the circular pore openings, while the cross-sectional views (c, d) reveal conical pore geometry. The cone-angle ( $\beta$ ) of the conical pores in thermal  $\text{SiO}_2$  (c) is approximately 1.8 times less than that in PECVD  $\text{SiO}_2$  (d).

three representative non-overlapping pores are highlighted in Figure 1a,b. Their average radius at the sample surface (T1, T2, and T3) are measured to be  $100.3 \pm 1.3$ ,  $103.2 \pm 1.6$ , and  $102.4 \pm 2.6$  nm, respectively, in thermal  $\text{SiO}_2$ . In contrast, the representative pores (P1, P2, and P3) in PECVD  $\text{SiO}_2$  measure  $127.2 \pm 2.7$ ,  $112.3 \pm 2.4$ , and  $114.7 \pm 1.6$  nm, respectively. The uncertainty values result from challenges in precisely defining nanopore boundaries due to charging effects during SEM imaging (see Figure 1). To address this, four cross-sectional measurements were taken across each pore and averaged. The standard deviation of these measurements provides the reported uncertainty values. Although only three pores are shown, they illustrate the larger size variation in PECVD  $\text{SiO}_2$  compared to the uniform pore size in thermal  $\text{SiO}_2$ . From SEM measurements, the standard deviation in the pore radius was measured to be  $\approx 1.8$  nm for thermal  $\text{SiO}_2$  but  $\approx 8$  nm for PECVD  $\text{SiO}_2$ . The reader must note that, unless otherwise noted, the nanopore radius or size mentioned throughout this work refers specifically to the radius of the cone base. To overcome the limited sampling of pores in SEM imaging, we complemented the microscopy analysis with small-angle X-ray scattering, which

provides statistically robust measurements, averaging over more than  $10^7$  pores during an experiment.

Cross-sectional SEM images (Figure 1c,d) reveal distinct differences in nanopore geometry between thermal and PECVD  $\text{SiO}_2$ . The full cone angle ( $\beta$ ) in PECVD  $\text{SiO}_2$  ( $\approx 44^\circ$ ) is approximately 1.8 times larger than in thermal  $\text{SiO}_2$  ( $\approx 26^\circ$ ). As described in our track etching model [13], the cone angle depends only on the ratio of the track-etch rate to the bulk-etch rate. Hence, the different angles indicate different etch-rate ratios for PECVD and thermal  $\text{SiO}_2$ . This discrepancy is not unexpected because PECVD-deposited films typically differ in morphology, density, and stoichiometry compared to thermally grown  $\text{SiO}_2$ . The electronic energy loss ( $S_e$ ) in the thermal and PECVD  $\text{SiO}_2$  layers was calculated using the SRIM2008 code [49]. The average  $S_e$  values for thermal  $\text{SiO}_2$  for 1.6 GeV, 185 MeV, and 89 MeV Au irradiation are 21.1, 16.6, and 12.1 keV/nm respectively, remaining almost constant throughout the film ( $\Delta S_e \leq 0.5\%$ ). Similarly, the average  $S_e$  values for PECVD  $\text{SiO}_2$  for 1.6 GeV, 185 MeV, and 89 MeV Au irradiation are 20.6, 16.3, and 11.8 keV/nm respectively, also with minimal varia-

tion across the film ( $\Delta S_e \leq 0.5\%$ ). The calculations for PECVD  $\text{SiO}_2$  thin films used values for the density and composition from our previous study [47]. In both layers, the projected ranges when irradiated with 185 and 89 MeV Au ions were  $\approx 20 \mu\text{m}$  and  $\approx 14 \mu\text{m}$ , respectively, whereas the projected ranges for thermal and PECVD  $\text{SiO}_2$  irradiated with 1.6 GeV were calculated to be  $\approx 87 \mu\text{m}$  and  $\approx 9 \mu\text{m}$ , respectively. Given that both the projected ranges and stopping powers are comparable for thermal and PECVD  $\text{SiO}_2$  layers, these parameters do not account for the observed differences in the shape of the fabricated nanopores.

To quantify the bulk etch rates, we measured the thickness etched from each film after etching in 3% HF for different defined time intervals. The thickness difference before and after etching was measured using ellipsometry, which revealed that thermal  $\text{SiO}_2$  is etched at  $15.6 \pm 0.6 \text{ nm/min}$ , while PECVD  $\text{SiO}_2$  is etched at  $34.3 \pm 1.2 \text{ nm/min}$ . Since the cone shape depends only on the ratio of track to bulk etch rate, the significantly different cone angles cannot be explained solely by the variation in bulk etch rates. Therefore, the track etch rate must also differ between the two types of  $\text{SiO}_2$ . Using our track etching model [13] and the measured pore radii, we estimate track etch rates of  $69 \pm 3 \text{ nm/min}$  for thermal and  $90 \pm 6 \text{ nm/min}$  for PECVD  $\text{SiO}_2$ , respectively.

While the scanning electron microscopy images reveal the variation in nanopore size for PECVD  $\text{SiO}_2$  compared to thermal  $\text{SiO}_2$ , as well as differences in nanopore morphology, these images do not provide robust statistical information and are

prone to measurement errors. Cross-sectional SEM imaging provides limited statistical reliability as the probability of cleaving directly through a nanopore's central axis is extremely low. This sampling bias introduces significant uncertainties in dimensional measurements and makes it challenging to obtain robust structural information about the nanopores. Figure 2 shows a representative 2D scattering pattern obtained from conical nanopores in thermal  $\text{SiO}_2$ . This image represents the simultaneous measurement of approximately  $10^7$  parallel nanopores, tilted by  $\approx 20^\circ$  with respect to the X-ray beam. Although fitting the entire image can give precise information on the nanopore size and cone angle, fitting the size distribution is computationally too expensive [29]. Our new approach of fitting the scattering intensities uses two orthogonal 1D cuts of the scattering image (Figure 2). This analysis preserves the high precision of SAXS analysis while substantially reducing computational demands and enabling investigation of the size distributions. Figure 2 highlights the regions selected for horizontal and vertical cuts. The resulting scattering intensity profiles (vertical cut: orange and horizontal cut: blue) from these cuts are shown on the right-hand side of Figure 2. The intensity values obtained at different tilt angles were fitted as described below.

Figure 3 presents 2D scattering images for thermal (Figure 3a) and PECVD (Figure 3b)  $\text{SiO}_2$ . As indicated by the yellow arrows in Figure 3a, clear secondary scattering features can be observed in thermal  $\text{SiO}_2$ , indicative for a low dispersity in nanopore dimensions. In contrast, these features are absent in PECVD  $\text{SiO}_2$ . We ascribe this effect to the variation in

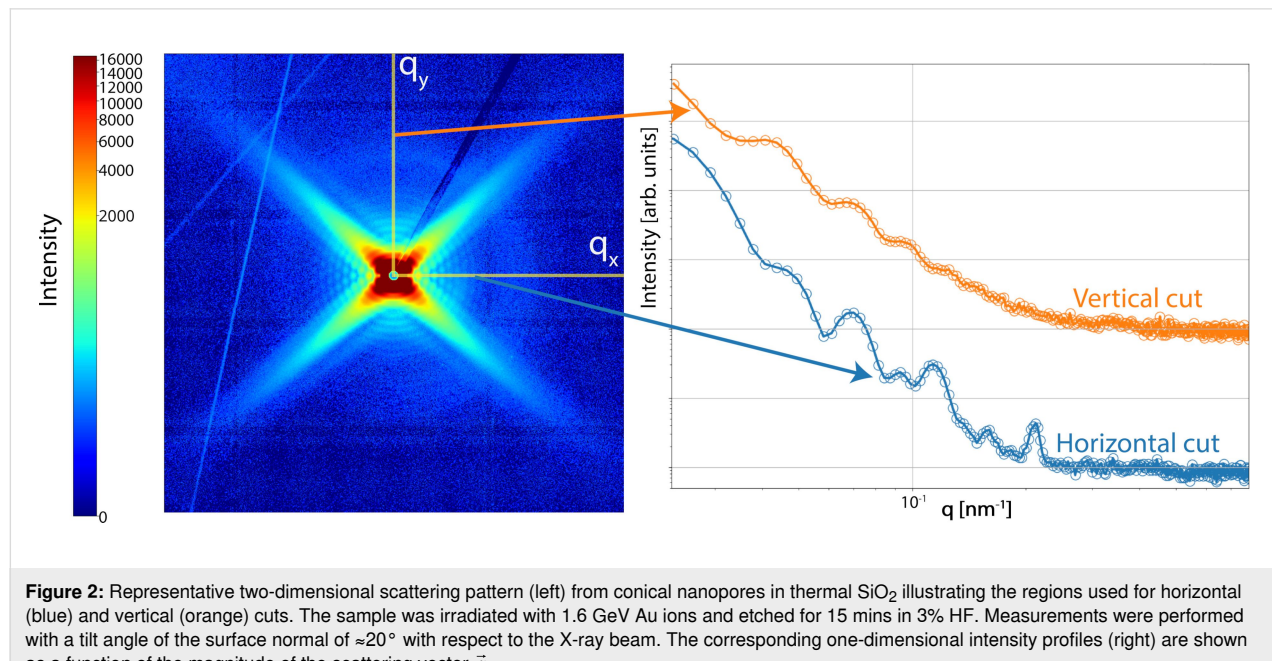


**Figure 2:** Representative two-dimensional scattering pattern (left) from conical nanopores in thermal  $\text{SiO}_2$  illustrating the regions used for horizontal (blue) and vertical (orange) cuts. The sample was irradiated with 1.6 GeV Au ions and etched for 15 mins in 3% HF. Measurements were performed with a tilt angle of the surface normal of  $\approx 20^\circ$  with respect to the X-ray beam. The corresponding one-dimensional intensity profiles (right) are shown as a function of the magnitude of the scattering vector  $\vec{q}$ .

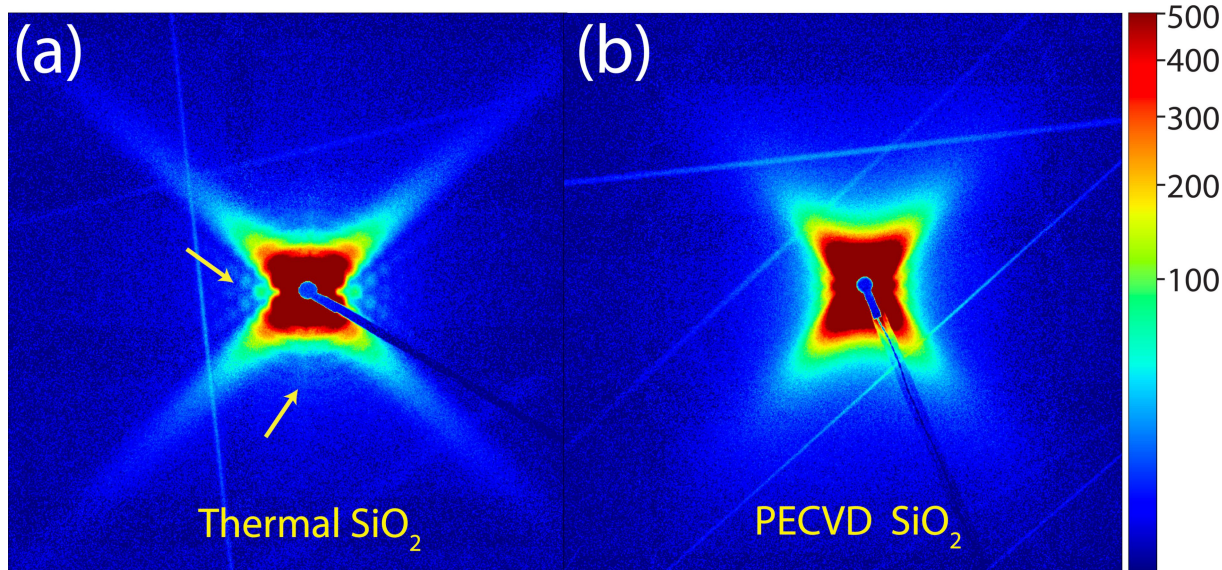


**Figure 3:** Two-dimensional small-angle X-ray scattering (SAXS) patterns of conical nanopores in thermal (a) and PECVD (b)  $\text{SiO}_2$  produced from irradiation of thin film samples with 1.6 GeV Au ions and etching with 3% HF, shown using the same intensity-contrast scale. The arrows in (a) highlight secondary scattering features that are more pronounced in thermal  $\text{SiO}_2$  than in the PECVD sample, consistent with a higher polydispersity of pore sizes in the latter.

nanopore size, as each pore generates a slightly different scattering intensity, effectively smearing out the secondary features. Furthermore, the absence of secondary features makes it difficult to fit the SAXS data using our 2D fitting model [29].

The scattering intensities from vertical and horizontal cuts of 2D SAXS images were analyzed for both PECVD and thermal  $\text{SiO}_2$  samples using the methodology detailed in the Experimental and Theory section. Figure 4 presents the experimental data and the corresponding model fits, where Figure 4a,b represents data from nanopores in thermal  $\text{SiO}_2$  and Figure 4c,d shows data from nanopores in PECVD  $\text{SiO}_2$ . Horizontal cuts are shown in Figure 4a,c, while vertical cuts at various tilt angles are shown in Figure 4b,d. The fitting models demonstrate excellent agreement with the experimental data across all scattering curves. Both samples were irradiated with 1.6 GeV Au ions and subsequently etched in 3% HF. For comparative analysis, we selected samples with similar nanopore radii: Thermal  $\text{SiO}_2$  (etched for 12 min) yielded pores of average radius 141.3 nm, while PECVD  $\text{SiO}_2$  (etched for 7 min) produced pores of average radius 154.2 nm. The PECVD samples exhibited nanopores of high quality, with a size distribution of  $\approx 8.3\%$ . While this size distribution is narrow compared to many nanopore systems [50], thermal  $\text{SiO}_2$  nanopores show an even narrower size distribution of only  $\approx 2.1\%$ . The higher dispersity observed in PECVD-based nanopores could be the result of defects or localized variations in material properties. While thermal  $\text{SiO}_2$  typically exhibits high homogeneity in local material properties,

factors such as the etching process and the ion irradiation energy straggling may introduce an effective narrow size distribution of pores. Although we apply a Schulz–Zimm distribution to model the nanopore radius, as described in the Experimental and Theory section, this distribution strongly correlates with variations in the cone angle. We can thus ascribe the polydispersity directly to the variation of the cone angles as well. The influence of size distribution on the scattering patterns is evident upon detailed examination. The horizontal cut intensities from thermal  $\text{SiO}_2$  nanopores reveal six to eight distinct oscillations, whereas PECVD  $\text{SiO}_2$  displays a maximum of four oscillations. Furthermore, the reduced peak-to-trough amplitude in oscillations resulting from nanopores in PECVD  $\text{SiO}_2$  corroborates the broader size distribution obtained from our fitting analysis. The reduced number of oscillations in PECVD  $\text{SiO}_2$  1D scattering intensity corresponds to the absence of secondary scattering features in the 2D scattering image as described above.

Figure 5 presents the evolution of half cone angle (Figure 5a), percentage polydispersity (Figure 5b), and nanopore radius (Figure 5c) as a function of etching time for nanopores in PECVD and thermal  $\text{SiO}_2$  irradiated with Au ions at different energies. The analysis reveals distinct differences between the two types of  $\text{SiO}_2$ . Nanopores in PECVD  $\text{SiO}_2$  exhibit on an average  $\approx 1.8$  times larger cone angles compared to the pores in thermal  $\text{SiO}_2$ . Moreover, the size distribution of nanopores, quantified by the polydispersity values (Figure 5b), are higher

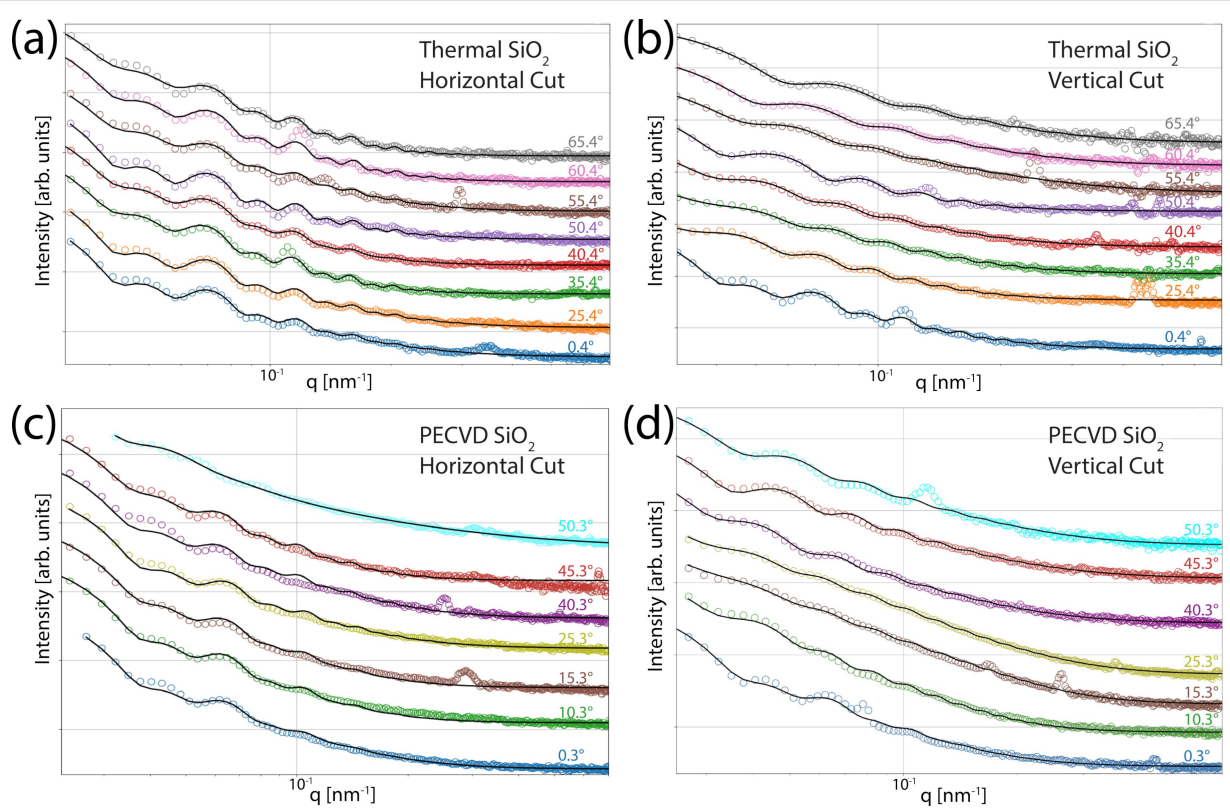


**Figure 4:** One-dimensional SAXS profiles of ion-irradiated thermal (a, b) and PECVD (c, d)  $\text{SiO}_2$ , extracted along the horizontal (a, c) and vertical (b, d) directions. Each pattern corresponds to a different tilt angle (labels in degrees), offset vertically for clarity. The solid lines denote model fits based on conical and core-transition models.

( $\approx 8\text{--}18\%$ ) in PECVD  $\text{SiO}_2$  compared to ( $\approx 2\text{--}4\%$ ) in thermal  $\text{SiO}_2$ . We note that compared to many other systems, the pore size homogeneity in thermal  $\text{SiO}_2$  is exceptional. In PECVD  $\text{SiO}_2$  samples, nanopores fabricated using 185 MeV Au ion irradiation show slightly larger cone angles compared to those created with 89 MeV and 1.6 GeV Au ions. This variation may result from sample-to-sample difference that can arise from the PECVD deposition processes, as the samples originated from different deposition runs. The 185 MeV-fabricated nanopores also exhibited the highest polydispersity, underscoring the variability in PECVD film characteristics. The validity of our analysis is supported by multiple cross-validation measures. The cone angle values derived from 1D fits for thermal  $\text{SiO}_2$  not only agree well with those obtained from the established 2D fitting model [29] but also correspond well with the cross-sectional SEM images. Furthermore, polydispersity values determined by SAXS correlate strongly with the estimates from scanning electron microscopy analysis. It is important to emphasize that SAXS analysis provides a statistically robust characterization of polydispersity, radius, and cone angle values by sampling over  $10^6$  nanopores – a population size unattainable through microscopy analysis. A linear fit of the nanopore radius versus etching time yielded radial etching rates of  $21.1 \pm 0.8$ ,

$21.1 \pm 0.2$ , and  $22.1 \pm 0.2$  nm/min for PECVD  $\text{SiO}_2$  nanopores fabricated using 1.6 GeV, 185 MeV, and 89 MeV Au ions, respectively. In contrast, thermal  $\text{SiO}_2$  exhibited a lower radial etching rate of  $11.9 \pm 0.1$  nm/min. Using these values in conjunction with our track etching model [13], we calculated track etching rates of  $85 \pm 10$ ,  $87 \pm 5$ , and  $91 \pm 6$  nm/min for the respective PECVD samples, while thermal  $\text{SiO}_2$  showed a track etching rate of  $68 \pm 4$  nm/min. These track etching rates agrees well with the values calculated using radii from SEM images and employing our track etching model.

## Conclusion

In this study, we performed a comparative analysis of conical nanopores fabricated in thermal and PECVD  $\text{SiO}_2$  using ion track etching employing SEM and SAXS. Our findings reveal substantial differences in the track etching rate and the bulk etching rate between these materials, which in turn affect the nanopore geometry. Nanopores in PECVD  $\text{SiO}_2$  exhibit cone angles approximately 1.8 times larger than those in thermally grown  $\text{SiO}_2$  – a variation attributable to differences in material density, composition, and stoichiometry between the two oxide types. Furthermore, thermal  $\text{SiO}_2$  demonstrates remarkable homogeneity (polydispersity  $\approx 2\text{--}4\%$ ) compared to PECVD

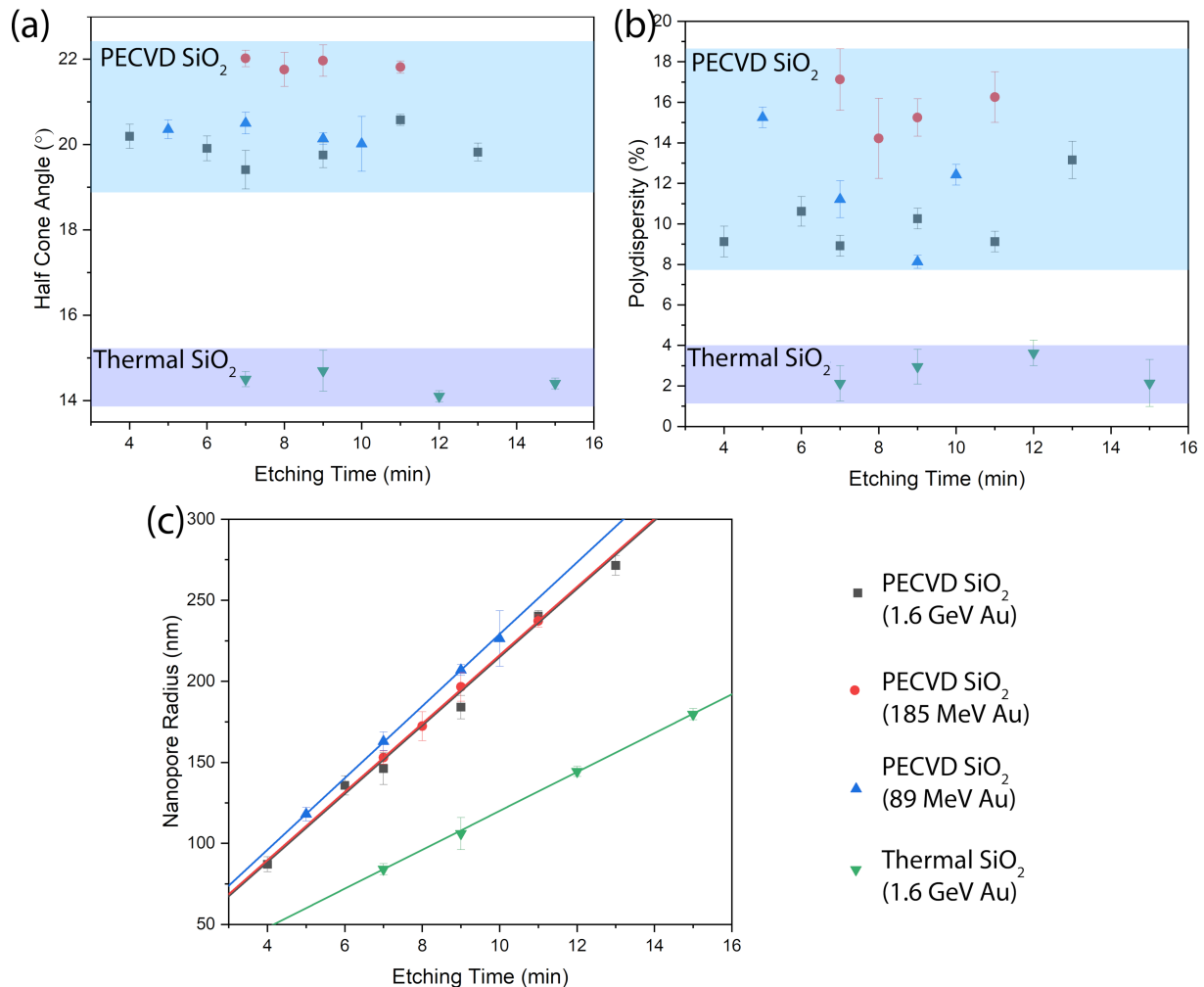


**Figure 5:** Half cone angle (a), percentage polydispersity (b), and nanopore radius (c) as functions of etching time for conical nanopores in thermal and PECVD  $\text{SiO}_2$ , irradiated with Au ions at different energies. The shaded regions in (a) and (b) highlight approximate parameter ranges for thermal versus PECVD  $\text{SiO}_2$ . In (c), solid lines represent linear fits to the data.

$\text{SiO}_2$  (polydispersity  $\approx 8\text{--}18\%$ ). Although PECVD  $\text{SiO}_2$  nanopores show broader size distributions, these values still represent a significant improvement over existing nanoporous systems reported in the literature [50] as the pore distributions can exceed 50% in existing systems. The use of different  $\text{SiO}_2$  compositions allows for tuning of the pore geometry, which can have a significant influence on performance in different applications [35,51-53].

The new analytical methodology developed and employed in this study marks a pronounced advancement in conical nanopore characterization. This approach enables reliable assessment of size distributions while maintaining high precision in the determination of nanopore shape, thereby facilitating a detailed investigation of the relationships between fabrication conditions and resultant pore characteristics. The ability

to quantify the size distribution with high accuracy is particularly valuable, as size uniformity often plays a crucial role in the performance of nanopore-based applications.

## Experimental and Theory

### Nanopore formation in thermal and PECVD $\text{SiO}_2$

We utilized two types of amorphous silicon dioxide samples. The first type consisted of 1  $\mu\text{m}$  thick thermally grown  $\text{SiO}_2$  on  $\langle 100 \rangle$  Si substrates (300  $\mu\text{m}$  thickness), obtained commercially from WaferPro Ltd, USA. The second type comprised PECVD-deposited  $\text{SiO}_2$  films ( $\approx 1.1 \mu\text{m}$  thick) grown on a 300  $\mu\text{m}$  thick, polished  $\langle 100 \rangle$  Si substrates using an Oxford Plasmalab 100 PECVD system. PECVD deposition was performed at 650  $^{\circ}\text{C}$  with gas flow rates of 16 sccm  $\text{SiH}_4$ , 980 sccm  $\text{N}_2$ , and 14 sccm

$\text{NH}_3$ . Ellipsometry measurements employing a Tauc–Lorentz model revealed a deposition rate of  $\approx 36.6$  nm/min.

Both sample types were irradiated with Au ions of 1.6 GeV at the UNILAC accelerator (GSI Helmholtzzentrum für Schwerionenforschung GmbH, Germany). Additionally, the PECVD  $\text{SiO}_2$  samples were irradiated with 89 and 185 MeV Au ions at the 14UD accelerator (Heavy Ion Accelerator Facility, Australian National University). The irradiation fluences ranged from  $1 \times 10^8$  to  $5 \times 10^8$  ions· $\text{cm}^{-2}$ , ensuring minimal overlap between ion tracks and resulting nanopores [13,54,55].

To convert the ion tracks into nanopores, the samples were etched at room temperature in 3% hydrofluoric acid for varying durations. The etching process was stopped by removing samples from the etchant followed by three successive rinses in de-ionized water, each lasting 30 s, after which the samples were air dried. The scanning electron microscopy images of the nanopores were obtained using a FEI Verios 460 microscope. For cross-sectional images, the samples were cleaved and imaged vertically.

### Small angle X-ray scattering

Transmission small angle X-ray scattering (SAXS) measurements were conducted at the SAXS/WAXS beamline at the Australian Synchrotron, Melbourne, with a photon energy of 12 keV. The samples were measured as is, and the Si substrate was not removed before SAXS measurements. The sample-to-detector distances ranged between 7.2 and 7.6 m. Data collection was performed using Pilatus 1M and Pilatus 2M detectors during different measurement cycles. A silver behenate (AgBeh) standard was used to calibrate both the sample-to-detector distance and beam center positions. Exposure times ranged from 2 to 10 s, with samples mounted on a three-axis goniometer for precise alignment with the incident X-ray beam. Detailed information regarding alignment, tilts, measurements, geometry, and 2D analysis procedures can be found in our previous works [29,40].

The 2D scattering patterns were converted into 1D scattering intensities through horizontal and vertical cuts (along  $q_x$  and  $q_y$ , respectively) originating from the center of the beamstop. We selected the cut with minimal interference from the Kossel line by comparing the symmetric positive and negative values  $q_x$  and  $q_y$  relative to the center of the beam. These cuts were obtained through azimuthal integration along the masked region (see Figure 2). To preserve the accuracy of polydispersity measurements without averaging interference effects, the cuts were kept as narrow as practicable. For analysis of the vertical cut, we employed our previously reported cone model [29], where the form factor is given by:

$$f_{2D}(q_r, q_z) = C \int_0^L J_1(r_z, q_r) \frac{r_z}{q_r} \exp(-i, z, q_z) dz. \quad (1)$$

Here,  $f_{2D}(q_r, q_z)$  represents the form factor assuming rotational symmetry along the Z axis of the conical nanopores,  $L$  is the length of the conical nanopores,  $J_1$  denotes the first-order Bessel function, and  $C$  accounts for electron density contrast and other constant parameters. The radial component of the scattering vector ( $\vec{q}$ ), denoted as  $q_r$ , is given by  $\sqrt{q_x^2 + q_y^2}$ . For the vertical cut analysis, we set  $q_x = 0$ , which reduces  $q_r$  to  $q_y$ . This formulation captures the scattering amplitude for conical objects while accounting for the radius variation along the Z axis. The horizontal cut analysis was performed setting  $q_y = 0$ . Equation 1 then reduces to a “core transition” model, previously detailed in our work [21,56]. This model incorporates a constant core radius (fixed to the ion track radius determined by SAXS [13,47,57]) with a linear density transition region. The corresponding form factor is expressed as:

$$f_{CT}(q_r, q_z) = 4\pi \frac{\sin(q_z l)}{q_z} \frac{\pi}{(q_r)^2} \times \begin{bmatrix} -R_C J_1(R_C q_r) H_0(R_C q_r) \\ + (R_C + R_T) J_1((R_C + R_T) q_r) H_0((R_C + R_T) q_r) \\ + R_C J_0(R_C q_r) H_1(R_C q_r) \\ - (R_C + R_T) J_0((R_C + R_T) q_r) H_1((R_C + R_T) q_r) \end{bmatrix}, \quad (2)$$

where  $R_C$  represents the fixed core radius matching the ion track radius,  $R_T$  denotes the transition region thickness, and  $H_u(z)$  represents the Struve function given by:

$$H_u(z) = \left(\frac{z}{2}\right)^{u+1} \sum_{m=0}^{\infty} \frac{(-1)^m \left(\frac{z}{2}\right)^{2m}}{\Gamma\left(m + \frac{3}{2}\right) \Gamma\left(m + u + \frac{3}{2}\right)}. \quad (3)$$

To measure the distribution of the nanopore sizes, we implemented a narrow Schulz–Zimm distribution [13,21,47,56]. Readers are referred to these works for detailed information on the implementation of polydispersity. The fits are performed using a custom C- and Python-based code that employs a non-linear least-squares algorithm. To correct for background scattering originating from the, among others, air and the substrate, we employ a  $q$ -dependent background [26] as it is not feasible to extract and subtract the background explicitly for these materials systems.

We fit the horizontal cuts to determine the nanopore radii and the corresponding size distribution. The oscillations in the scattering intensity along the horizontal cuts remain the same as a

function of the tilt angle between cone axis and X-ray beam, making it impossible to extract direct information about the cone angles. In contrast, the scattering intensities in the vertical cuts vary with the tilt angle and provide information on the cone angle of the nanopores. As the cone angle and tilt angle are highly correlated, fitting just a single vertical cut produces large uncertainties mainly because of the challenges in accurately determining the experimental tilt angle [29,40]. Therefore, we acquire scattering images at multiple tilt angles and fit the resulting scattering intensities simultaneously.

Our overall fitting strategy proceeds as follows. For each sample, first, we fit the scattering intensities from individual horizontal cuts obtained at different tilt angles to obtain initial estimates of nanopore radii. Next, multiple horizontal cuts originating from different tilt angles are fitted together to refine the radius values and determine size dispersity more accurately. We then used these refined values as starting points for simultaneously fitting multiple vertical cuts, treating the tilt angle as a variable to account for the imperfect alignment of the cones with the incoming X-rays. It should be noted that the difference in different tilt angles is fixed and known for different experiments. Finally, we combine both horizontal and vertical cuts in a single simultaneous fit, constraining the radius and the cone angle to the same values.

## Acknowledgements

Part of the research was undertaken at the SAXS/WAXS beamline at the Australian Synchrotron, part of ANSTO, and we thank the beamline scientists for their technical assistance. We also acknowledge access to the NCRIS (National Collaborative Research Infrastructure Strategy) supported Heavy-Ion Accelerator facility (the 14UD accelerator) at the Australian National University. The results presented here are based on a UMAT experiment that was carried out on the UNILAC X0 beamline at the GSI Helmholtz Center for Heavy Ion Research, Darmstadt (Germany) in the frame of FAIR Phase-0. This work used the ACT node of the NCRIS-enabled Australian National Fabrication Facility (ANFF-ACT).

## Funding

The authors acknowledge financial support from the Australian Research Council (ARC) under the ARC Discovery Project Scheme.

## Author Contributions

Shankar Dutt: conceptualization; formal analysis; investigation; methodology; software; visualization; writing – original draft. Rudradeep Chakraborty: formal analysis; investigation. Christian Notthoff: investigation; methodology; software; writing – review & editing. Pablo Mota-Santiago: investigation; writing –

review & editing. Christina Trautmann: investigation; writing – review & editing. Patrick Kluth: conceptualization; funding acquisition; investigation; methodology; supervision; visualization; writing – review & editing.

## ORCID® IDs

Shankar Dutt - <https://orcid.org/0000-0002-6814-070X>

Pablo Mota-Santiago - <https://orcid.org/0000-0002-1537-4318>

Christina Trautmann - <https://orcid.org/0000-0001-7058-6340>

Patrick Kluth - <https://orcid.org/0000-0002-1806-2432>

## Data Availability Statement

Data generated and analyzed during this study is available from the corresponding author upon reasonable request.

## Preprint

A non-peer-reviewed version of this article has been previously published as a preprint: <https://doi.org/10.48550/arXiv.2502.14118>

## References

1. Xue, L.; Yamazaki, H.; Ren, R.; Wanunu, M.; Ivanov, A. P.; Edel, J. B. *Nat. Rev. Mater.* **2020**, *5*, 931–951. doi:10.1038/s41578-020-0229-6
2. He, Y.; Tsutsui, M.; Zhou, Y.; Miao, X.-S. *NPG Asia Mater.* **2021**, *13*, 48. doi:10.1038/s41427-021-00313-z
3. Yeh, H.-C.; Chang, C.-C.; Yang, R.-J. *Phys. Rev. E* **2015**, *91*, 062302. doi:10.1103/physreve.91.062302
4. Zhao, X.; Qin, H.; Tang, M.; Zhang, X.; Qing, G. *TrAC, Trends Anal. Chem.* **2024**, *173*, 117658. doi:10.1016/j.trac.2024.117658
5. Wanjiya, M.; Zhang, J.-C.; Wu, B.; Yin, M.-J.; An, Q.-F. *Desalination* **2024**, *578*, 117441. doi:10.1016/j.desal.2024.117441
6. Dutt, S.; Apel, P.; Lizunov, N.; Notthoff, C.; Wen, Q.; Trautmann, C.; Mota-Santiago, P.; Kirby, N.; Kluth, P. *J. Membr. Sci.* **2021**, *638*, 119681. doi:10.1016/j.memsci.2021.119681
7. Dutt, S.; Karawdeniya, B. I.; Bandara, Y. M. N. D. Y.; Afrin, N.; Kluth, P. *Anal. Chem. (Washington, DC, U. S.)* **2023**, *95*, 5754–5763. doi:10.1021/acs.analchem.3c00023
8. Wei, X.; Penkauskas, T.; Reiner, J. E.; Kennard, C.; Uline, M. J.; Wang, Q.; Li, S.; Aksimentiev, A.; Robertson, J. W. F.; Liu, C. *ACS Nano* **2023**, *17*, 16369–16395. doi:10.1021/acsnano.3c05628
9. Meyer, N.; Abrao-Nemeir, I.; Janot, J.-M.; Torrent, J.; Lepoittevin, M.; Balme, S. *Adv. Colloid Interface Sci.* **2021**, *298*, 102561. doi:10.1016/j.cis.2021.102561
10. Siwy, Z. S.; Bruening, M. L.; Howorka, S. *Chem. Soc. Rev.* **2023**, *52*, 1983–1994. doi:10.1039/d2cs00894g
11. Varongchayakul, N.; Song, J.; Meller, A.; Grinstaff, M. W. *Chem. Soc. Rev.* **2018**, *47*, 8512–8524. doi:10.1039/c8cs00106e
12. Lu, W.; Cao, Y.; Qing, G. *Chem. – Asian J.* **2022**, *17*, e202200675. doi:10.1002/asia.202200675
13. Dutt, S.; Notthoff, C.; Wang, X.; Trautmann, C.; Mota-Santiago, P.; Kluth, P. *Appl. Surf. Sci.* **2023**, *628*, 157370. doi:10.1016/j.apsusc.2023.157370
14. Pan, J.; Xu, W.; Zhang, Y.; Ke, Y.; Dong, J.; Li, W.; Wang, L.; Wang, B.; Meng, B.; Zhou, Q.; Xia, F. *Nano Energy* **2024**, *132*, 110412. doi:10.1016/j.nanoen.2024.110412

15. Zhang, H.; Tian, Y.; Jiang, L. *Nano Today* **2016**, *11*, 61–81. doi:10.1016/j.nantod.2015.11.001

16. Mohammad, A. W.; Teow, Y. H.; Ang, W. L.; Chung, Y. T.; Oatley-Radcliffe, D. L.; Hilal, N. *Desalination* **2015**, *356*, 226–254. doi:10.1016/j.desal.2014.10.043

17. Calvo, J. I.; Bottino, A.; Capannelli, G.; Hernández, A. J. *Membr. Sci.* **2004**, *239*, 189–197. doi:10.1016/j.memsci.2004.02.038

18. Kanani, D. M.; Fissell, W. H.; Roy, S.; Dubnisheva, A.; Fleischman, A.; Zydner, A. L. *J. Membr. Sci.* **2010**, *349*, 405–410. doi:10.1016/j.memsci.2009.12.003

19. Dutt, S.; Shao, H.; Karawdeniya, B.; Bandara, Y. M. N. D. Y.; Daskalaki, E.; Suominen, H.; Kluth, P. *Small Methods* **2023**, *7*, 2300676. doi:10.1002/smtd.202300676

20. Li, N.; Yu, S.; Harrell, C. C.; Martin, C. R. *Anal. Chem. (Washington, DC, U. S.)* **2004**, *76*, 2025–2030. doi:10.1021/ac035402e

21. Wang, X.; Dutt, S.; Notthoff, C.; Kiy, A.; Mota-Santiago, P.; Mudie, S. T.; Toimil-Molares, M. E.; Liu, F.; Wang, Y.; Kluth, P. *Phys. Chem. Chem. Phys.* **2022**, *24*, 9345–9359. doi:10.1039/d1cp05813d

22. Sun, C.; Zhu, S.; Liu, M.; Shen, S.; Bai, B. *J. Phys. Chem. Lett.* **2019**, *10*, 7188–7194. doi:10.1021/acs.jpcllett.9b02715

23. DesOrmeaux, J. P. S.; Winans, J. D.; Wayson, S. E.; Goborski, T. R.; Khire, T. S.; Striemer, C. C.; McGrath, J. L. *Nanoscale* **2014**, *6*, 10798–10805. doi:10.1039/c4nr03070b

24. Wang, L.; Wang, Z.; Patel, S. K.; Lin, S.; Elimelech, M. *ACS Nano* **2021**, *15*, 4093–4107. doi:10.1021/acsnano.0c08628

25. Wang, X.; Luo, Y.; Huang, K.; Cheng, N. *Adv. Agrochem* **2022**, *1*, 3–6. doi:10.1016/j.aac.2022.08.002

26. Kiy, A.; Notthoff, C.; Dutt, S.; Grigg, M.; Hadley, A.; Mota-Santiago, P.; Kirby, N.; Trautmann, C.; Toimil-Molares, M. E.; Kluth, P. *Phys. Chem. Chem. Phys.* **2021**, *23*, 14231–14241. doi:10.1039/d1cp02063c

27. Rastgar, M.; Moradi, K.; Burroughs, C.; Hemmati, A.; Hoek, E.; Sadrzadeh, M. *Chem. Rev.* **2023**, *123*, 10156–10205. doi:10.1021/acs.chemrev.3c00168

28. Tsutsui, M.; Yoshida, T.; Yokota, K.; Yasaki, H.; Yasui, T.; Arima, A.; Tonomura, W.; Nagashima, K.; Yanagida, T.; Kaji, N.; Taniguchi, M.; Washio, T.; Baba, Y.; Kawai, T. *Sci. Rep.* **2017**, *7*, 17371. doi:10.1038/s41598-017-17443-6

29. Hadley, A.; Notthoff, C.; Mota-Santiago, P.; Dutt, S.; Mudie, S.; Carrillo-Solano, M. A.; Toimil-Molares, M. E.; Trautmann, C.; Kluth, P. *Phys. Rev. Mater.* **2020**, *4*, 056003. doi:10.1103/physrevmaterials.4.056003

30. Kiy, A.; Dutt, S.; Notthoff, C.; Toimil-Molares, M. E.; Kirby, N.; Kluth, P. *ACS Appl. Nano Mater.* **2023**, *6*, 8564–8573. doi:10.1021/acsam.3c00960

31. Liu, Z.; Ma, L.; Zhang, H.; Zhuang, J.; Man, J.; Siwy, Z. S.; Qiu, Y. *ACS Appl. Mater. Interfaces* **2024**, *16*, 30496–30505. doi:10.1021/acsami.4c02078

32. Vlassiour, I.; Apel, P. Y.; Dmitriev, S. N.; Healy, K.; Siwy, Z. S. *Proc. Natl. Acad. Sci. U. S. A.* **2009**, *106*, 21039–21044. doi:10.1073/pnas.0911450106

33. Dutt, S.; Karawdeniya, B.; Bandara, Y. M. N. D. Y.; Kluth, P. *Future Sci. OA* **2024**, *10*, 2340882. doi:10.2144/fsoa-2023-0226

34. Ma, C.; Yeung, E. S. *Anal. Chem. (Washington, DC, U. S.)* **2010**, *82*, 478–482. doi:10.1021/ac902487c

35. Balannec, B.; Ghoufi, A.; Szymczyk, A. J. *Membr. Sci.* **2018**, *552*, 336–340. doi:10.1016/j.memsci.2018.02.026

36. Zhang, Y.; Schatz, G. C. *J. Phys. Chem. Lett.* **2017**, *8*, 2842–2848. doi:10.1021/acs.jpcllett.7b01137

37. Lin, C.-Y.; Combs, C.; Su, Y.-S.; Yeh, L.-H.; Siwy, Z. S. *J. Am. Chem. Soc.* **2019**, *141*, 3691–3698. doi:10.1021/jacs.8b13497

38. Duleba, D.; Dutta, P.; Denuga, S.; Johnson, R. P. *ACS Meas. Sci. Au* **2022**, *2*, 271–277. doi:10.1021/acsmmeasuresci.1c00062

39. Hellborg, R.; Whitlow, H. J.; Zhang, Y., Eds. *Ion Beams in Nanoscience and Technology; Particle Acceleration and Detection*; Springer: Berlin, Heidelberg, 2010. doi:10.1007/978-3-642-00623-4

40. Hadley, A.; Notthoff, C.; Mota-Santiago, P.; Hossain, U. H.; Kirby, N.; Toimil-Molares, M. E.; Trautmann, C.; Kluth, P. *Nanotechnology* **2019**, *30*, 274001. doi:10.1088/1361-6528/ab10c8

41. Apel, P. Y.; Dmitriev, S. N. *Adv. Nat. Sci.: Nanosci. Nanotechnol.* **2011**, *2*, 013002. doi:10.1088/2043-6262/2/1/013002

42. Apel, P. *Nucl. Instrum. Methods Phys. Res., Sect. B* **2003**, *208*, 11–20. doi:10.1016/s0168-583x(03)00634-7

43. Liu, F.; Wang, M.; Wang, X.; Wang, P.; Shen, W.; Ding, S.; Wang, Y. *Nanotechnology* **2019**, *30*, 052001. doi:10.1088/1361-6528/aaed6d

44. Hanot, H.; Ferain, E. *Nucl. Instrum. Methods Phys. Res., Sect. B* **2009**, *267*, 1019–1022. doi:10.1016/j.nimb.2009.02.011

45. Kaya, D.; Keçeci, K. *J. Electrochem. Soc.* **2020**, *167*, 037543. doi:10.1149/1945-7111/ab67a7

46. Price, P. B. *Radiat. Meas.* **2008**, *43*, S13–S25. doi:10.1016/j.radmeas.2008.04.002

47. Mota-Santiago, P.; Vazquez, H.; Bierschenk, T.; Kremer, F.; Nadzri, A.; Schauries, D.; Djurabekova, F.; Nordlund, K.; Trautmann, C.; Mudie, S.; Ridgway, M. C.; Kluth, P. *Nanotechnology* **2018**, *29*, 144004. doi:10.1088/1361-6528/aaabdb

48. Karouta, F.; Vora, K.; Tian, J.; Jagadish, C. *J. Phys. D: Appl. Phys.* **2012**, *45*, 445301. doi:10.1088/0022-3727/45/44/445301

49. Ziegler, J. F.; Ziegler, M. D.; Biersack, J. P. *Nucl. Instrum. Methods Phys. Res., Sect. B* **2010**, *268*, 1818–1823. doi:10.1016/j.nimb.2010.02.091

50. Sutariya, B.; Karan, S. *Sep. Purif. Technol.* **2022**, *293*, 121096. doi:10.1016/j.seppur.2022.121096

51. Ramirez, P.; Apel, P. Y.; Cervera, J.; Mafé, S. *Nanotechnology* **2008**, *19*, 315707. doi:10.1088/0957-4484/19/31/315707

52. Pietschmann, J.-F.; Wolfram, M.-T.; Burger, M.; Trautmann, C.; Nguyen, G.; Pevarnik, M.; Bayer, V.; Siwy, Z. *Phys. Chem. Chem. Phys.* **2013**, *15*, 16917–16926. doi:10.1039/c3cp53105h

53. Laohakunakorn, N.; Thacker, V. V.; Muthukumar, M.; Keyser, U. F. *Nano Lett.* **2015**, *15*, 695–702. doi:10.1021/nl504237k

54. Riedel, C.; Spohr, R. *Radiat. Eff.* **1979**, *42*, 69–75. doi:10.1080/10420157908201738

55. Kluth, P.; Schnohr, C. S.; Sprouster, D. J.; Byrne, A. P.; Cookson, D. J.; Ridgway, M. C. *Nucl. Instrum. Methods Phys. Res., Sect. B* **2008**, *266*, 2994–2997. doi:10.1016/j.nimb.2008.03.182

56. Dutt, S.; Apel, P.; Polezhaeva, O.; Kiy, A.; Afrin, N.; Notthoff, C.; Kirby, N.; Kluth, P. *Polymer* **2023**, *282*, 126133. doi:10.1016/j.polymer.2023.126133

57. Kluth, P.; Schnohr, C. S.; Pakarinen, O. H.; Djurabekova, F.; Sprouster, D. J.; Giulian, R.; Ridgway, M. C.; Byrne, A. P.; Trautmann, C.; Cookson, D. J.; Nordlund, K.; Toulemonde, M. *Phys. Rev. Lett.* **2008**, *101*, 175503. doi:10.1103/physrevlett.101.175503

## License and Terms

This is an open access article licensed under the terms of the Beilstein-Institut Open Access License Agreement (<https://www.beilstein-journals.org/bjnano/terms>), which is identical to the Creative Commons Attribution 4.0 International License (<https://creativecommons.org/licenses/by/4.0>). The reuse of material under this license requires that the author(s), source and license are credited. Third-party material in this article could be subject to other licenses (typically indicated in the credit line), and in this case, users are required to obtain permission from the license holder to reuse the material.

The definitive version of this article is the electronic one which can be found at:

<https://doi.org/10.3762/bjnano.16.68>